Combined Numerical and Experimental Studies on the Dynamic and Quasi-static Failure Modes of Brittle Rock

Chunjiang Zou[1, 2*] and Li Huanqiang[2,3]

[1] *Department of Civil Engineering, Monash University, Australia*

[2] *Previously in School of Civil and Environmental Engineering, Nanyang Technological University, Singapore*

[3] *Zhejiang Provincial Institute of Communications Planning, Design & Research, China*

[*]Corresponding author, E-mail address: chunjiang.zou@monash.edu

Abstract

Loading rate affects not only the mechanical properties of rock but also the cracking behaviour or the failure mode. Firstly, experimental studies on the mechanical properties and the related cracking behaviour are studied based on the Carrara marble specimens containing a pre-existing flaw under different loading rates. The result shows that both the compressive and tensile strengths are rate-dependent but with different sensitivities to strain rate. Meanwhile, the cracking processes of the single-flawed specimens are also found to be rate-dependent with the aid of an ultra-high-speed video system. Secondly, to investigate the mechanism behind the experimental phenomena, a material model based on the experimental strength data is proposed and applied to the numerical model. The influence of the rate-dependent strength on the cracking behaviour is studied comprehensively by using the 2D and 3D explicit dynamic FEM code. The numerical results reveal how the rate-dependent strength affects fracturing behaviour and the failure stress of the single-flawed specimen. The plastic zones do not equal the damaged zone or the cracks. The dynamic loadings lead to the “X” shaped failure mode of the single-flawed specimen regardless of the flaw inclination angle. In contrast, the quasi-static loadings lead to the diagonal failure mode. It indicates that shear displacement dominates the whole cracking process under dynamic loadings, while it only dominates the failure period under quasi-static loadings.

Keywords: Rock dynamics; failure criterion; SHPB; crack; numerical simulation; strain rate

1. Introduction

In earth sciences, planetary sciences and rock engineerings, impact loading or shaking and its influence on rocks are usually related and discussed, e.g. earthquake, meteorite impact, volcano eruption, landslide, tunnel rockburst and engineering blasting. The high and ultra-high loading rate, which can be as high as 10^4 s^{-1} in rock blasting and 10^9 or higher in meteorite impact, is encountered in these natural and engineering activities [1, 2]. The slip rate in an earthquake can be as high as several meters per second[3], producing an acceleration exceeding 20 m/s^2. In this case, for a limited length of shear contact zone or asperity, the shear strain rate or the compressive strength rate can be very high. The shear rupture propagation speed can be higher than the shear wave speed for more than 2000 m/s [4-6]. But the generated loading rate decreases rapidly with the distance. To better understand the rock and lithosphere behaviours under dynamic loadings, the rate-dependent mechanical properties and failure processes of rocks are required to evaluate the failure of geological bodies. On the other side, the failure mode of geological bodies can help to back analyze the force resource (plate movement, earthquake, volcano eruption or meteorite impact). In engineering, the influence of rock blasting wave on the neighbouring tunnel, cavern and underground structures cannot be neglected[7, 8]. The stability of tunnel, cavern and underground structures under severe earthquake or explosions is also a focus of rock dynamics [9-12].

In solid material mechanics, the mechanical properties of many brittle materials are dependent on the loading rate. Most construction materials and rocks are investigated to be sensitive to the loading rate for the mechanical properties [13, 14]. Rock shows its rate-dependence of mechanical properties ranging from quasi-static regime to the dynamic regime. Strength, fracture toughness and brittleness of rock or rock-like materials were reported to be affected by the loading rate, but to different extents [15-25].

The dynamic strength of rocks has been studied by using various laboratory tests, e.g. drop weight test [26-28], impact test [29-31], and split Hopkinson pressure bar test [16, 32-40]. Dynamic compressive strengths of rock-like materials are more extensively studied than dynamic tensile strengths, shear strengths and dynamic fracture toughness due to a more complicated experimental setup needed for these tests. However, these less-studied properties of rocks have also been found to be loading rate-dependent to various extents [20, 24, 37, 41-44].

Since the material properties influence the cracking behaviour, crack initiation and propagation should also be rate-dependent. Although this concept is generally accepted, there have been limited investigations on the cracking behaviour of rocks under dynamic loadings, and on the influence of rate-dependent mechanical properties on cracking behaviour. Previous literature on the dynamic crack behaviour generally concentrated on crack speed[45], fragmentation [46-48], fracture toughness [49] and the spalling phenomena [46]. Since intact rock always containing micro-defects or micro-cracks and rock masses are typically fractured or jointed, the rock specimens, which is cut open flaws at the center, are usually modelled to study the rock fracturing processes under different loading conditions. Rock or rock-like specimens with artificial flaws has been studied by experimental approaches and numerical simulations under quasi-static [50-52] and dynamic loadings [53-57]. The authors have investigated the dynamic cracking behaviour of marble using a single-flawed specimen with different flaw inclination angle by experimental methods [58-60].

Carrara marble, which is a commonly used material to physically simulate the mechanical properties and failure process of rocks or rock masses[61-65], is used to fabricate the specimens in the present study. One essential phenomenon associated with the cracking behaviour of such marble is the appearance of white patches before the initiation of visible macro-cracks under both quasi-static and dynamic loadings [59, 61, 66, 67]. Some authors also named the white patch shear belt or white belt. This phenomenon makes the observation of the cracking process more informative. The origin of the white patch has not been confirmed. It is usually considered the severely stripped (even crushed) material of marble [66] or the deviation/failure of crystalline grains in marble [67]. Based on the microscopic investigation by the scanning electron microscope (SEM) and the nanoindentation technique [68, 69], the white patch is revealed to consist of zones with a variety of micro-cracks reducing the nanoindentation hardness and modulus.

Due to the limited sample rate of the data collection system and the high-speed propagation of the crack, as well as pulverization of specimens after dynamic tests, numerical modelling is developed to obtain more detailed information of the cracking process. By analyzing the simulation results, the physical relations between the rate-dependent strength and the dynamic fracturing modes can be explained in some ways. The dynamic FEM code – AUTODYN is a widely-used explicit FEM program in material dynamics research. Failure processes of both ductile and brittle materials have been simulated using this program by various researchers [70-

[74]. Li and Wong (2012) [70] investigated the application of AUTODYN in the simulation of rock fracturing processes under both quasi-static and dynamic loadings. Huang et al. (2015) studied the crack coalescence of a sandstone numerically using AUTODYN [75]. The present two-dimensional numerical study extends the previous works in the material model correlation with the experimental results and rate-dependent failure criterion.

In this numerical study, a strain rate-dependent constitutive model is developed for the Carrara marble based on the experimental results obtained in quasi-static and dynamic tests. Since the plastic deformation increase with the strain rate in the dynamic regime, the Drucker-Prager yield criterion (D-P criterion) has been used and modified to a strain rate dependent failure envelope here. D-P criterion is a pressure-dependent model for determining the failure of a material or undergoing plastic yielding, has been applied to various brittle materials, such as rocks, concrete and polymers [13, 71, 76-79]. To test the validity of the plain-strain assumption in 2D simulation, the 2D simulation results are compared with the 3D simulation results, which indicates that the 2D simulation can make a balance between simulation accuracy and efficiency. The numerical results generally agree with the experimental observations with respect to the fracturing phenomena under different loading conditions. Links between the rate-dependent mechanical properties and the different cracking processes are made. The results also verify the feasibility of this material model in the potential application into more practical rock engineering projects which are involved with high strain rate loadings.

2. Methodology

To minimize the size effect [80, 81], specimens, which are fabricated from Carrara marble slabs, are of the same dimensions and geometries. The dimensions and flaw configuration of the two-dimensional and three-dimensional numerical models are the same as those of the experimental specimens. The compressive and tensile strengths under various strain rate from quasi-static to dynamic regimes are determined from the uniaxial compression tests and Brazilian disc tests conducted on intact specimens, respectively. The test systems include a hydro-servo compression machine and a split Hopkinson pressure bar (SHPB) setup for quasi-static and dynamic tests, respectively[59, 82]. For the data processing, the quasi-static and dynamic strength is calculated based on the suggested methods by ISRM [83, 84, 38].

2.1 Experimental methodology

2.1.1 Experimental models

Figure 1 shows the dimensions of the rectangular specimen. An abrasive jet cutter cuts the pre-existing straight open flaw. The specimens with various flaw inclination angles θ, including 0°, 15°, 30°, 45°, 60°, 75°, and 90°, are studied in this paper. The specimen size effect and the friction between the specimen and the bar should be considered in evaluating the strength and cracking behaviours [25]. To minimize the size and end boundary friction effect to the cracking behaviour, the length to width ratio of 2:1 is used, and the different friction coefficients are used for quasi-static and dynamic simulations. The length is about 60 mm to make the specimen have the ability to undertake a higher strain rate.

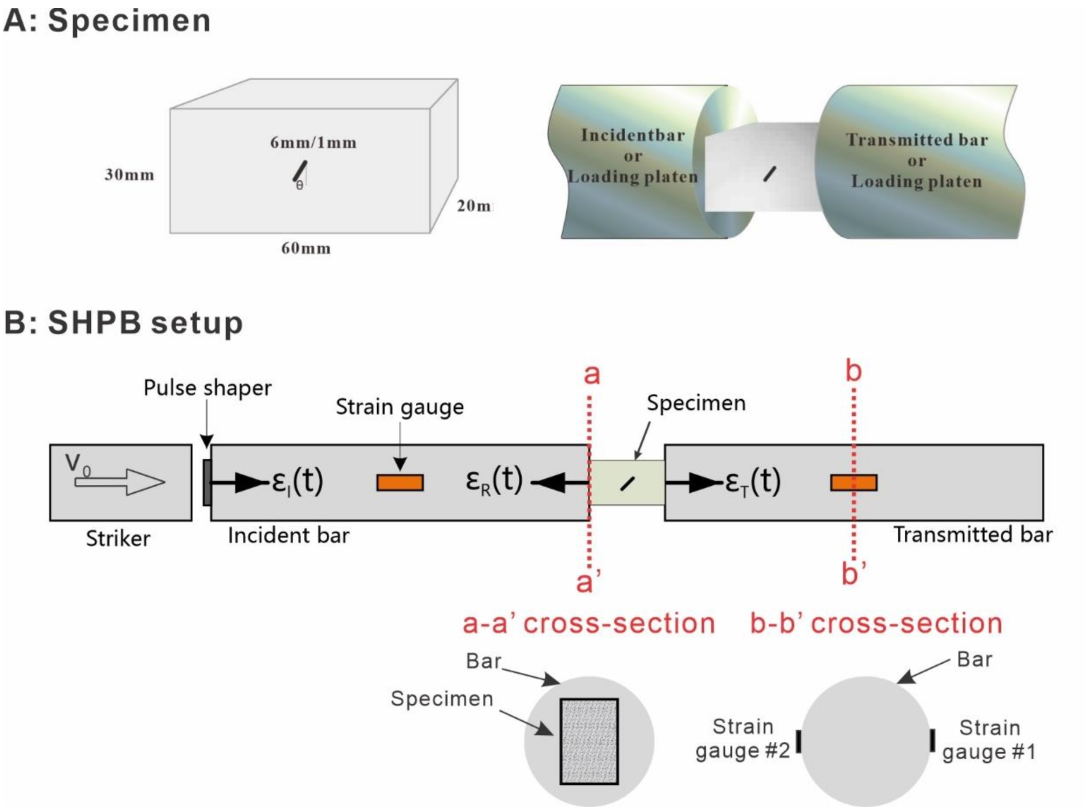

Figure 1 Dimensions of the single-flawed specimen (A) and the setup of SHPB (B)[59]

2.1.2 Loading conditions

The strain rates applied to the intact specimens to determine specimen strength are shown in **Table 1**. The quasi-static compressive strength, which is 90 MPa under a strain rate of 10^{-4} s^{-1}, refers to the average value in previously reported literature[61-65] and the tested value in the present study. In the tests on the single-flawed specimens, the quasi-static strain rate is 10^{-5} s^{-1}, and the dynamic value is around 150 s^{-1}.

Table 1 Strain rates applied on the intact specimens in different test types

Test type	Quasi-static Brazilian test	Dynamic Brazilian test	Quasi-static compression test	Dynamic compression test
Minimum strain rate (s^{-1})	10^{-7}	5	10^{-4}	100
Maximum strain rate (s^{-1})	10^{-4}	30	10^{-4}	600

The setup of the Split Hopkinson pressure bar (SHPB) system is also shown in **Figure 1**. A copper pulse shaper, which is clung on the left end of the incident bar, is used to reduce the wave dispersion effects and help achieve a better stress equilibrium condition. The high-speed video subsystem captures the specimen failure process at a frame rate of 40,000 frames per second.

2.1.3 Stress equilibrium

The satisfaction of the stress equilibrium state plays a crucial role in ensuring the data reliability of dynamic SHPB tests. All the specimens have achieved the stress equilibrium in the dynamic tests according to the ISRM suggested method. Two approaches are used to achieve the stress equilibrium condition in a specimen.

(1) Relatively short specimens are used. The critical strain rate $\dot{\varepsilon_m}$, which is the maximum allowed strain rate for the stress equilibrium state, is calculated according to the following equation [57, 69]:

$$\dot{\varepsilon_m} = \varepsilon_f c_s / \alpha L$$

where c_s is the wave velocity in the specimen, ε_f is the failure strain of the brittle materials, and L is the specimen length. The times of the reflection α are determined to be six for marble specimens, which is a conservative value calculated according to Ravichandran and Subhash (1994)[85].

For the present study, $\dot{\varepsilon_m}$ is calculated to be 167 s^{-1} for a 60 mm long Carrara marble specimen, while it is determined to be 500 s^{-1} for a 20 mm long specimen.

(2) A pulse shaper is used to promote a stress equilibrium state due to its relatively quick and easy deformation property[86-90]. It is normally a 1 mm or 2 mm thick copper with a diameter of 20 mm adhering to the end of the incident bar using grease.

2.1.4 White patch recognition

An image comparison program is used to help observe the subtle development of white patches in a white marble which is not easily distinguishable by unaided eyes. **Figure 2** shows a typically processed image by the image comparison software. The black dots represent those pixels experiencing a colour or greyscale change upon comparing two images.

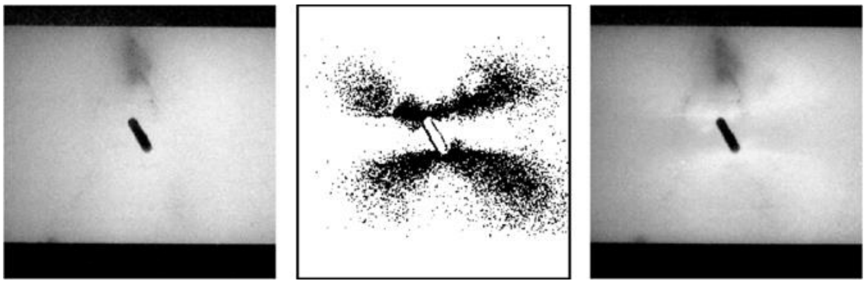

Figure 2 Processed high-speed image (middle) showing the pixel difference between the left (earlier) and right (later) images (flaw inclination angle 30°) [59]

2.2 Numerical models

The numerical model creates a new strain rate-dependent Drucker-Prager yield criterion for the Carrara marble based on the present experimental data. By using this strain rate-dependent yield criterion, the deformation and cracking processes in the rectangular specimen containing a single flaw subjected to the dynamic and quasi-static loading tests are simulated and compared with the experimental results. Quadrilateral isoparametric elements are used under the plane strain assumption.

Since the wave reflection and transmission can happen at the bar-specimen interfaces, the simulations of a dynamic loading system only considering the specimen or a system considering the specimen and short loading platen cannot comprehensively represent the SHPB testing system in previous numerical studies. The length of the incident and transmitter bars should also be long enough to minimize the undesirable wave superposition. Moreover, to achieve a satisfactory stress equilibrium, the half wavelength of the incident wave is preferred to have a size comparable to the bar length in the experimental study. Therefore, a full-size SHPB model is therefore established instead. For simplicity of the numerical calculation, the impact offered by the striking system is modelled as a time-history stress wave extracted from the experimental data. The material properties of the steel and Carrara marble used in the numerical models are shown in **Table 2**.

Table 2 Material properties obtained from experimental studies

Carrara marble	Poisson's ratio, v	0.19
	Young's modulus E	49 GPa
	Dry density, ρ	2.7 g/cm^3
	Bulk Modulus, K	26.3 GPa
	Shear Modulus, μ	20.6 GPa
Maraging steel	Density, ρ	8.1 g/cm^3
	Young's modulus E	210 GPa
	Poisson's ratio, v	0.3
	Bulk Modulus, K	175.0 GPa
	Shear Modulus, μ	80.8 GPa
	Yield tensile strength, σ_t	>1000 MPa

The numerical models of the quasi-static and the dynamic tests in the present study are shown in **Figure 3**. The geometries and dimensions of specimens in these two kinds of loading conditions are identical. Mixed rectangular and triangular mesh grids are used in the numerical models. The rectangular grid is applied to mesh the bars or loading platens, while the triangular meshing grid is used to mesh the specimen. The size of the mesh grid varies in the model to make a balance between the calculation load and the precision. The bars are meshed by the coarse grid due to their high strength and elastic modulus. A medium meshing grid is conducted to the specimen. The mesh around the flaw is refined again to keep the necessary details of stress and strain variation around the flaw tips.

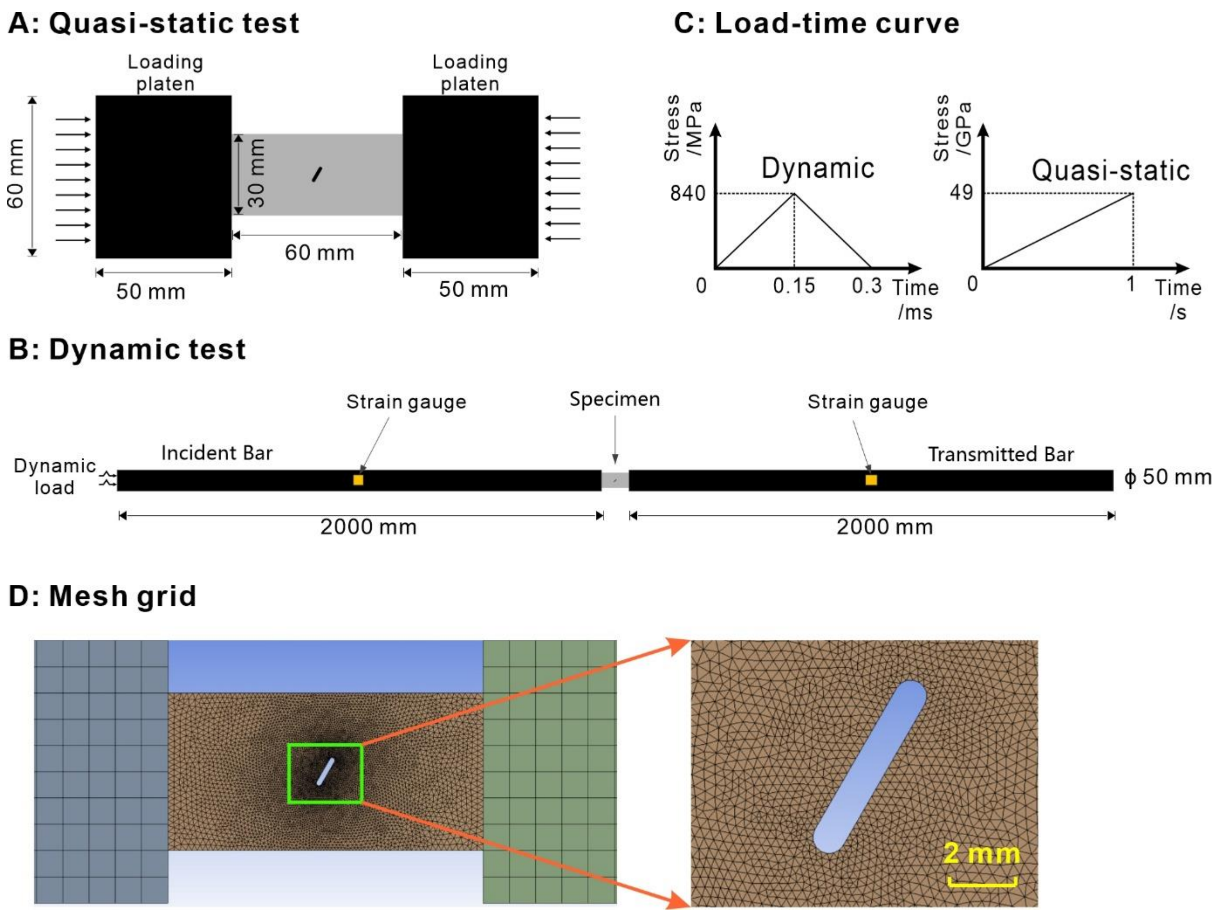

Figure 3 Numerical models and boundary conditions of quasi-static (A) and dynamic (B) tests as well as the input load-time curves (C) and mesh grid (D)

2.2.1 Dynamic Drucker-Prager yield criterion considering strain rate effect

The D-P criterion has the form

$$\sqrt{J_2} = A + BI_1 \qquad \textbf{Equation 1}$$

where I_1 is the first invariant of the Cauchy stress and J_2 is the second invariant of the deviatoric part of the Cauchy stress. The constants A and B are usually determined from either uniaxial or triaxial mechanical tests.

In the present study, the piece-wise Drucker-Prager strength criterion (D-P criterion) is used for the Carrara marble, while the linear elastic strength criterion is applied to the steel bar since the maximum stress in the test is much lower than the elastic limit. Since the marble strength generally varies with the strain rate, a strain-rate dependent D-P criterion is more suitable for the dynamic simulation. To avoid the massive computation in dynamic simulation, a constant strain rate loading is assumed to simplify the calculation. Thus, only one piece-wise D-P strength envelope is needed for a particular strain rate or loading rate, which significantly increases computation efficiency. The determination flow chart of the failure criterion is illustrated in **Figure 4.**

If σ_t is the yield stress in uniaxial tension,

$$\frac{1}{\sqrt{3}}\sigma_t = A + B\sigma_t \quad \textbf{Equation 2}$$

If σ_c is the yield stress in uniaxial compression,

$$\frac{1}{\sqrt{3}}\sigma_c = A - B\sigma_c \quad \textbf{Equation 3}$$

Then we can have the expression of A and B in this type:

$$A = \frac{2}{\sqrt{3}}\left(\frac{\sigma_c\sigma_t}{\sigma_c + \sigma_t}\right) \qquad B = \frac{1}{\sqrt{3}}\left(\frac{\sigma_t - \sigma_c}{\sigma_c + \sigma_t}\right) \quad \textbf{Equation 4}$$

Under dynamic strain rates, for a specific strain rate,

$$A_d = \frac{2}{\sqrt{3}}\left(\frac{\sigma_{cd}(\dot{\varepsilon})\sigma_{td}(\dot{\varepsilon})}{\sigma_{cd}(\dot{\varepsilon}) + \sigma_{td}(\dot{\varepsilon})}\right) \qquad B_d = \frac{1}{\sqrt{3}}\left(\frac{\sigma_{td}(\dot{\varepsilon}) - \sigma_{cd}(\dot{\varepsilon})}{\sigma_{cd}(\dot{\varepsilon}) + \sigma_{td}(\dot{\varepsilon})}\right) \quad \textbf{Equation 5}$$

Then, we have the dynamic Drucker-Prager strength criterion,

$$\sqrt{J_2} = A_d(\dot{\varepsilon}) + B_d(\dot{\varepsilon})I_1 \quad \textbf{Equation 6}$$

Since only uniaxial dynamic tests have been conducted on the marble in the present experimental study, a two-point linear D-P strength envelope is first determined. Then, to avoid the irrational strength increase in the linear envelope, the strength envelope becomes a gently sloping line when I_1 is higher than a certain level. This line is assumed to be parallel to the last segment of the quasi-static piece-wise strength envelope. The final failure envelope is shown in **Figure 6**.

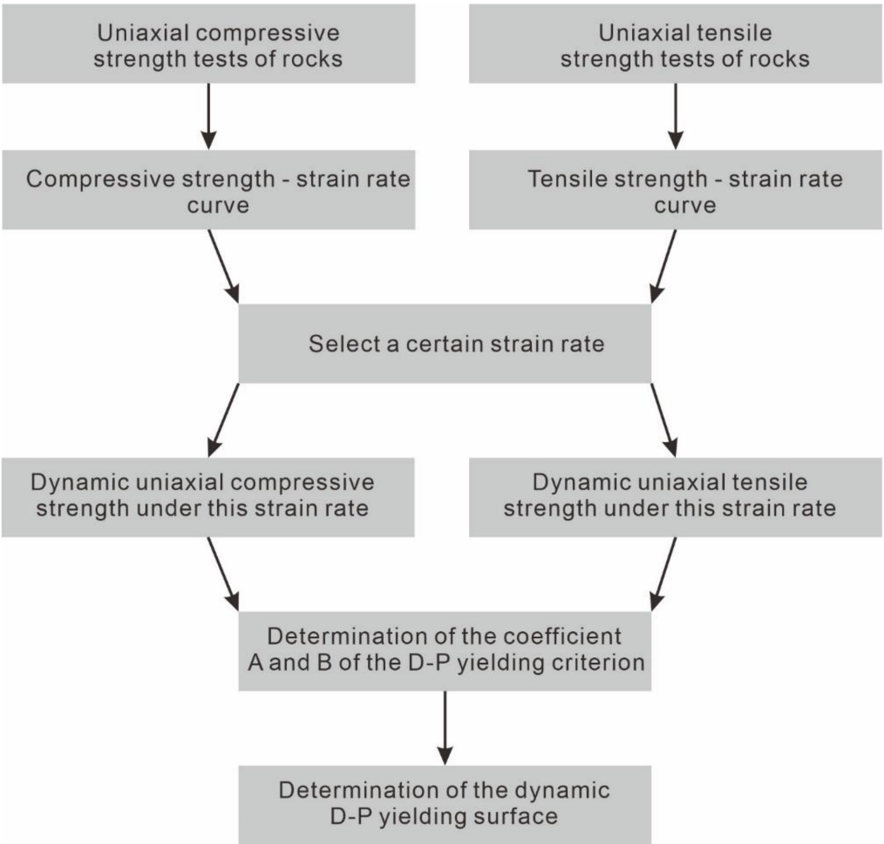

Figure 4 Flow chart of the dynamic D-P yielding surface determination under different strain rates

2.2.2 Cumulative damage failure model

The cumulative damage failure model is commonly utilized to describe the macroscopic inelastic behaviour of materials such as ceramics, concrete and rocks, the strength of which will be significantly reduced by crushing [91]. The isotropic post-failure response of materials is assumed for this failure model. When a cell of the material fails, it can no longer sustain any shear or any negative pressure. In progressive crushing, a damage factor '*D*' is used to model the reduction of elastic moduli and yield strength of the material. In the standard situation, *D* is zero for the material undergoing all plastic deformation, the effective plastic strain of which is less than a value named EPS1. When the effective plastic strain increases to a specific value EPS2, *D* reaches the maximum value D_{max} which is less than one. Between EPS1 and EPS2, *D* increases linearly with the effective plastic strain.

The mathematical expression of *D* is illustrated in **Equation 7**.

$$D = D_{max}\left(\frac{EPS - EPS1}{EPS2 - EPS1}\right) \quad \textbf{Equation 7}$$

A damage function for the damage factor D is used to model the reduction of material properties in the process of crushing. These mechanical properties include the bulk modulus, shear modulus and yield strength of the material. For the fully damaged material, the compressive strength reaches a residual, while the tensile strength becomes zero. The damaged yield strength Y_{dam} is determined from the original yield strength Y and factor D as follows:

$Y_{dam} = Y(1 - D)$ for a positive hydrostatic pressure p **Equation 8**

$Y_{dam} = Y(1 - \frac{D}{D_{max}})$ for a negative p **Equation 9**

In contrast, D is assumed to have no influence on the bulk modulus K and shear modulus G in compression. However, K and G in tension will decrease to zero progressively when the damage is complete or reaches the maximum value.

$K_{dam} = K \; and \; G_{dam} = G$ for a positive hydrostatic pressure p **Equation 10**

$K_{dam} = K\left(1 - \frac{D}{D_{max}}\right) \; and \; G_{dam} = G\left(1 - \frac{D}{D_{max}}\right)$ for a negative p **Equation 11**

2.2.3 Dynamic and quasi-static loading

Typical waveforms obtained from the SHPB test with the use of a pulse shaper have an approximately triangular shape of incident wave [59]. Therefore, the triangular loading curve is designed to simplify the numerical computation, as shown in **Figure 3**C. The strain rate of this loading curve is 150 s^{-1} which is the average value of the strain rates used in the present dynamic tests on the single-flawed specimens. Within the quasi-static regime, the strain rate effect on the mechanical properties is inconspicuous. A representative constant strain rate of 1 s^{-1} is assumed to increase the computation efficiency.

3. Experimental results

Typical fracturing processes of marble generally include the development of the white patches and the macro-cracks. The initiation and propagation of white patches, which play an essential role in the failure process, are therefore observed and discussed in detail. The fracturing processes of single-flawed marble specimens with seven differently-oriented inclination angles under both quasi-static and dynamic loading conditions are studied. The present experimental and numerical studies focus mainly on a typical specimen possessing a 30° flaw inclination angle in detail.

3.1 Compressive and tensile strength

In this study, the compressive and tensile strengths are first determined by the dynamic SHPB tests. Afterwards, the dynamic strength corresponding to a particular strain rate is used to determine the yielding surface under such strain rate. For quasi-static conditions, the piece-wise D-P yielding surface is derived from a series of triaxial compression tests reported in the previous literature [92], and Brazilian tensile tests concluded by the authors.

The compressive and tensile strengths of Carrara marble are obtained under various strain rates in the present study, as shown in **Figure 5**. Since the dynamic SHPB tests on the single-flawed marble specimens are conducted under strain rates ranging from 120 to 180 s^{-1}, a representative strain rate of 150 s^{-1} is selected for the dynamic D-P yielding surface. The average dynamic uniaxial compressive strength and the average dynamic tensile strength under such strain rate are 400.5 MPa and 73.1 MPa, respectively.

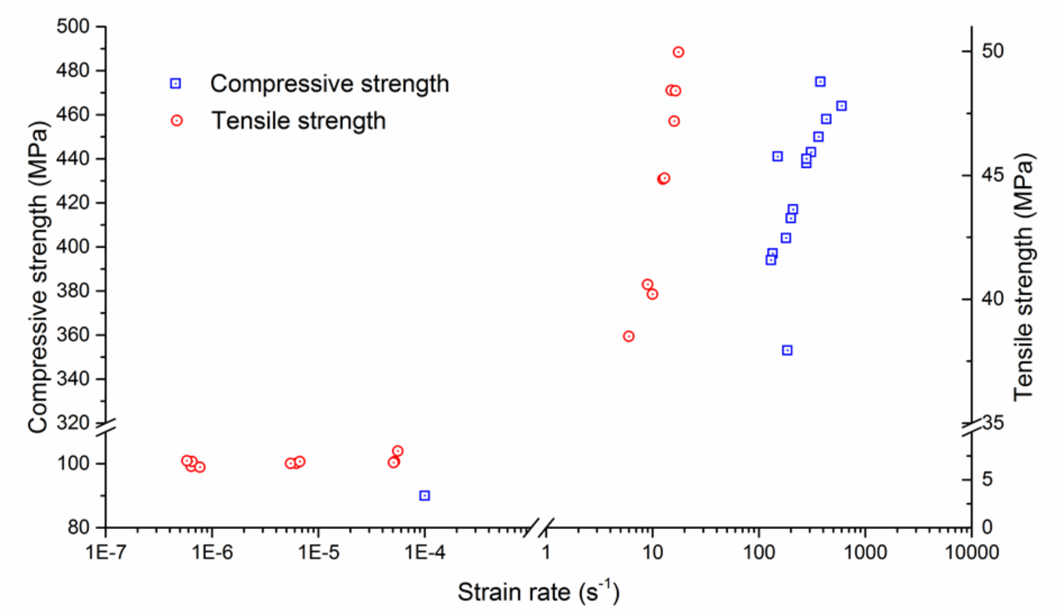

Figure 5 Experimental compressive and tensile strengths of Carrara marble under various strain rates (Note: Breaks are inserted in the axes for better visualization)

3.2 Quasi-static and dynamic D-P yielding surfaces

The quasi-static D-P yielding surface is derived from the data provided in **Figure 6**. The values of yielding stresses corresponding to various confining pressures are calculated, based on which the piece-wise quasi-static yielding surface is constructed. The dynamic D-P yielding envelope is also shown in the same figure. The corresponding strength values under such loading conditions are listed in **Table 3**.

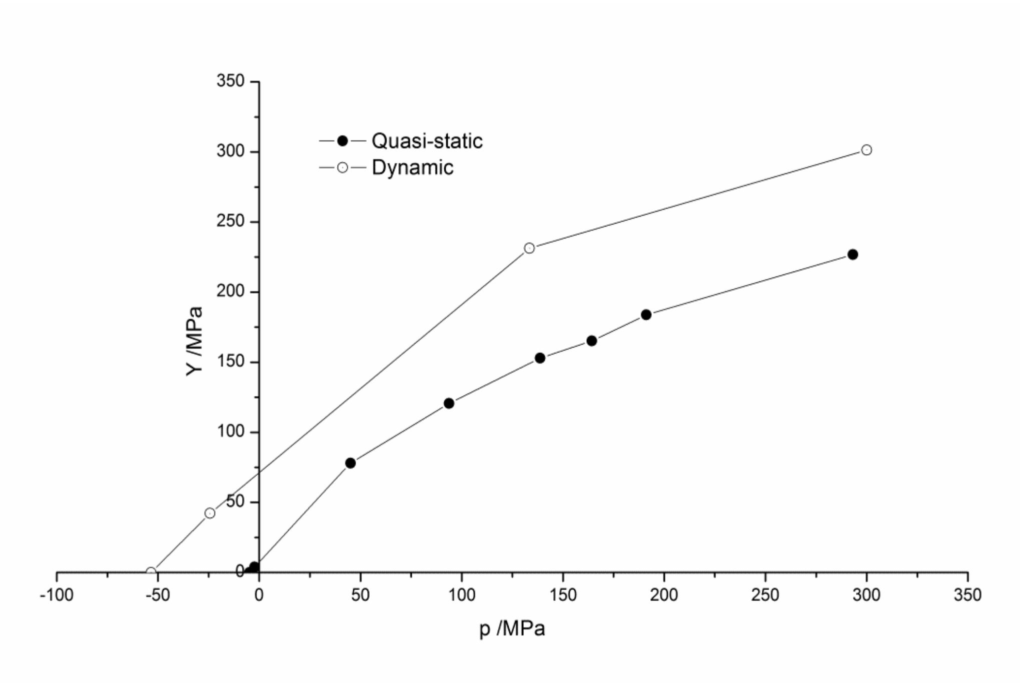

Figure 6 Piece-wise quasi-static D-P yielding surface and linear dynamic D-P yielding surface derived from the experimental data. The definitions of *p* and *Y* are shown in **Table 3**.

Table 3 Stress conditions of Carrara marble under the strain rate of 150 s^{-1} (I_1 is the first invariant of the Cauchy stress. J_2 is the second invariant of the deviatoric part of the Cauchy stress)

Specimen No.	σ_1 /MPa	σ_2 /MPa	σ_3 /MPa	$p = \frac{1}{3} I_1$ /MPa	$Y = \sqrt{J_2}$ /MPa
1	0	0	-73.1	-24.4	42.2
2	400.5	0	0	133.5	231.2

3.3 Fracturing processes of single-flawed marble specimens

3.3.1 White patch development

White patches develop earlier than the initiation of the macro-cracks in marble. In this section, the development of white patches and macro-cracks of the specimen containing an inclined flaw (β = 30°) under both quasi-static and dynamic loadings are described and discussed. The white patches initiated around the pre-existing flaw are also named the "first white patches". Three main types of white patches, namely tensile wing patches, shear patches and anti-wing patches (**Figure 7**), are commonly observed in the experiments. The nomenclature of the first patches is on the basis of the properties of macro-cracks that the white patches will eventually develop into. Wong and Einstein (2009) [93] summarised seven first crack types initiated around the single flaw under quasi-static loadings.

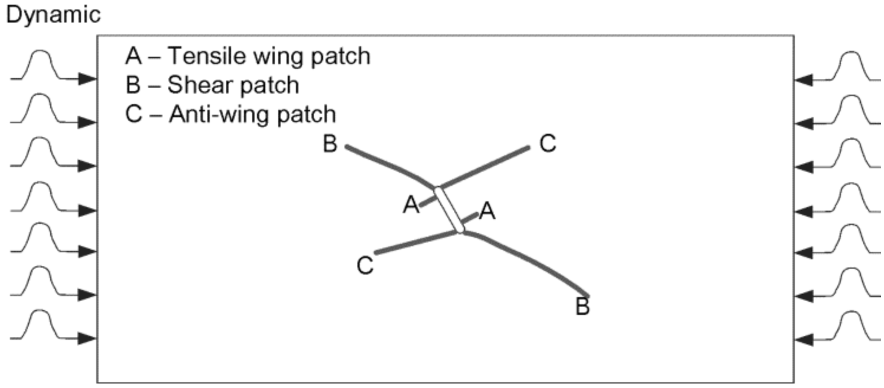

Figure 7 Three types of first white patches developed under dynamic loading [59]

For the specimen loaded dynamically, both the tensile wing patches and the shear patches initiate almost simultaneously around the flaw tips. For the specimen loaded quasi-statically, generally, the first white patches are very similar to those developed under dynamic loadings for the initiation position and the propagation direction at the early stage. The first white patches also include the tensile wing and shear patches.

The anti-wing patches as the secondary white patches also initiate around the flaw soon after the initiation of the first white patches under both quasi-static and dynamic loadings (**Figure 8**). The first and secondary patches constitute an 'X' shape pattern. This result indicates that the influence of the loading rate on the first and secondary white patches at the early stage of loading is very limited. However, some subtle differences are observed under these two loading conditions, including the time-lapse and the weight of white patches. The white patches of the dynamic tests occur at the very early stage of loading, while that of the quasi-static tests occur at the second half of loading.

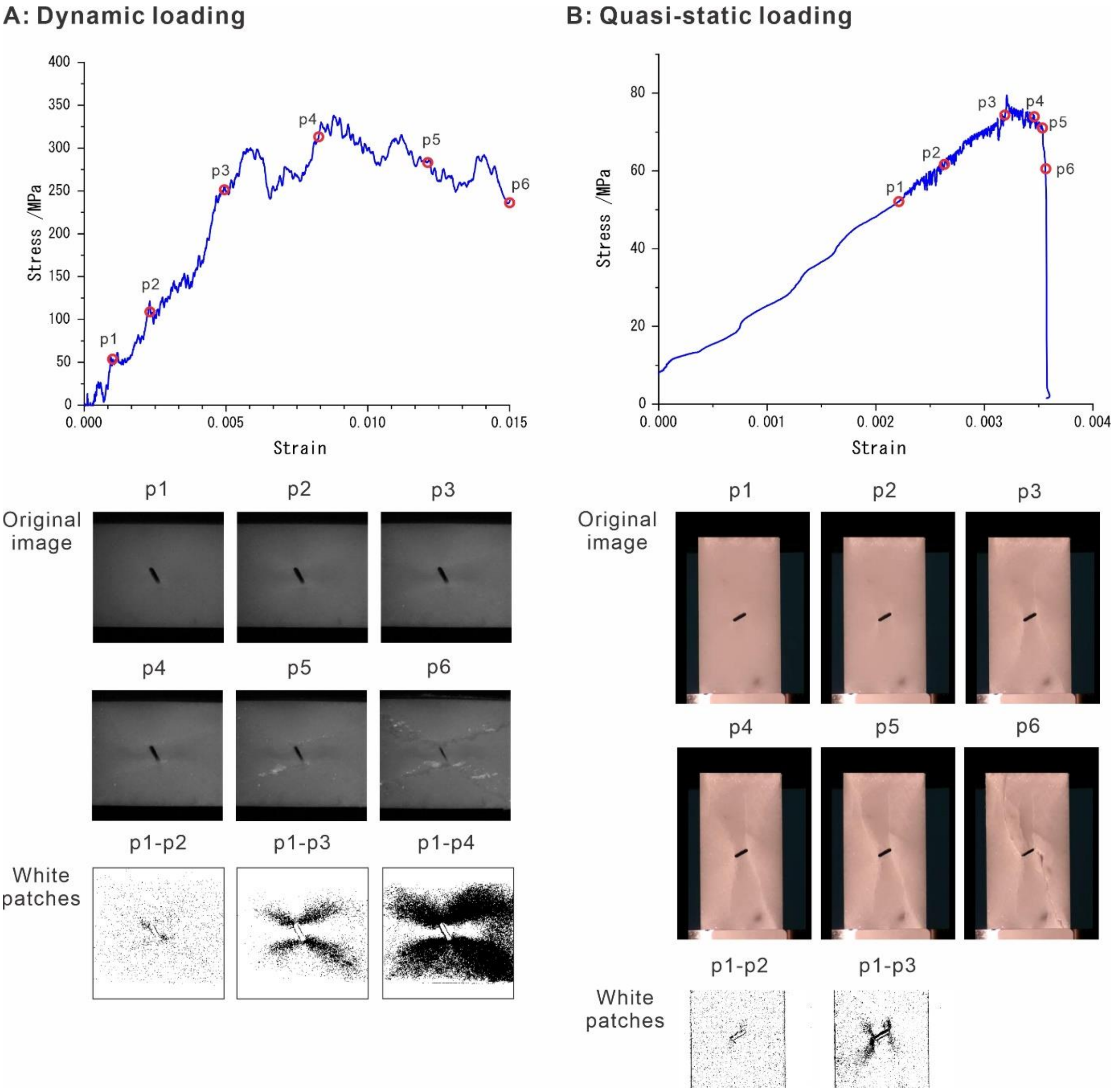

Figure 8 White patch and crack development in a single-flawed specimen under dynamic (A) and quasi-static (B) loadings. Top row – original images. Bottom row – processed images obtained from image comparison software (p1-pX means the comparison between p1 and pX).

3.3.2 Macro-cracks

In response to further loading, macro-cracks with visible aperture openings initiate along the trajectories of the previously initiated white patches. The future-developed macro-cracks share the same trajectories with the white patches (**Figure 9**). However, not all the white patches will evolve to the macro-cracks, which is generally observed in other single-flawed specimens with different inclination angles [59, 82]. In dynamic tests, one pair of the shear patches and another pair of anti-wing patches will evolve to an “X” shape crack pattern. No tensile wing patches will develop into any visible macro-cracks. In contrast, in quasi-static tests, only the anti-wing patches lead to the failure of the specimens.

As revealed from additional studies on specimens containing a flaw oriented at different inclination angles, the failure modes are also found to be significantly different under different loading rates. Under dynamic loading, two symmetrical pairs of shear cracks with an "X" shaped failure crack band lead to the specimen failure pattern. In contrast, under quasi-static loading, two major diagonal macro-cracks evolved from the anti-wing patches will cause the specimen failure regardless of the inclination angle. The complete crushing of the specimens appears after the peak stresses of the loading regardless of the loading rates.

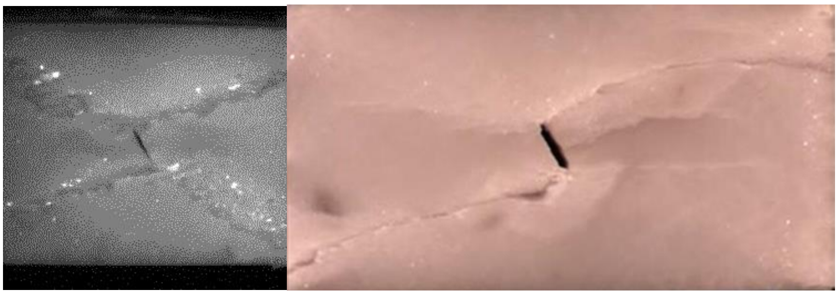

Figure 9 Failure modes of the specimens under dynamic (left, No. s20111220-4-30M) and quasi-static (right, No. 20121123-2-30) loadings. The crack tracks are highlighted in the right image.

4. Numerical results

In this section, numerical results of the mechanical responses of the specimen based on the material properties derived from the experiments are discussed. The cracking processes are illustrated and compared with the experimental results.

4.1 Model calibration

Two monitoring points are set in the numerical model of dynamic SHPB tests to record the stress histories of the incident and transmitter bars (**Figure 10**). The numerical stress histories are compared with the experimental ones. Due to the assumption of the ideal triangular incident wave in the numerical studies, the numerical stress histories appear to be smoother than the experimental ones. Generally, the numerical and experimental stress histories are similar to each other. However, due to the 2-D simulation nature and the lack of dynamic triaxial test results on the marble, the simulated peak stress (which is related to the compressive strength) of the transmitted wave is slightly less than the experimental one. Therefore, in the present study, the numerical result of the strain-stress curve has a lower magnitude compared with the experimental one. This shortage will be repaired and optimized by 3D simulation and more dynamic triaxial tests to establish a more accurate 3D Drucker-Prager criterion. But the dynamic peak stress of the specimen is several times higher than the quasi-static peak stress (**Figure 11**), which is consistent with the experimental behaviour. Therefore, in the strain-stress curves, the relative position of each cracking event can be considered and analyzed in dynamic failure processes.

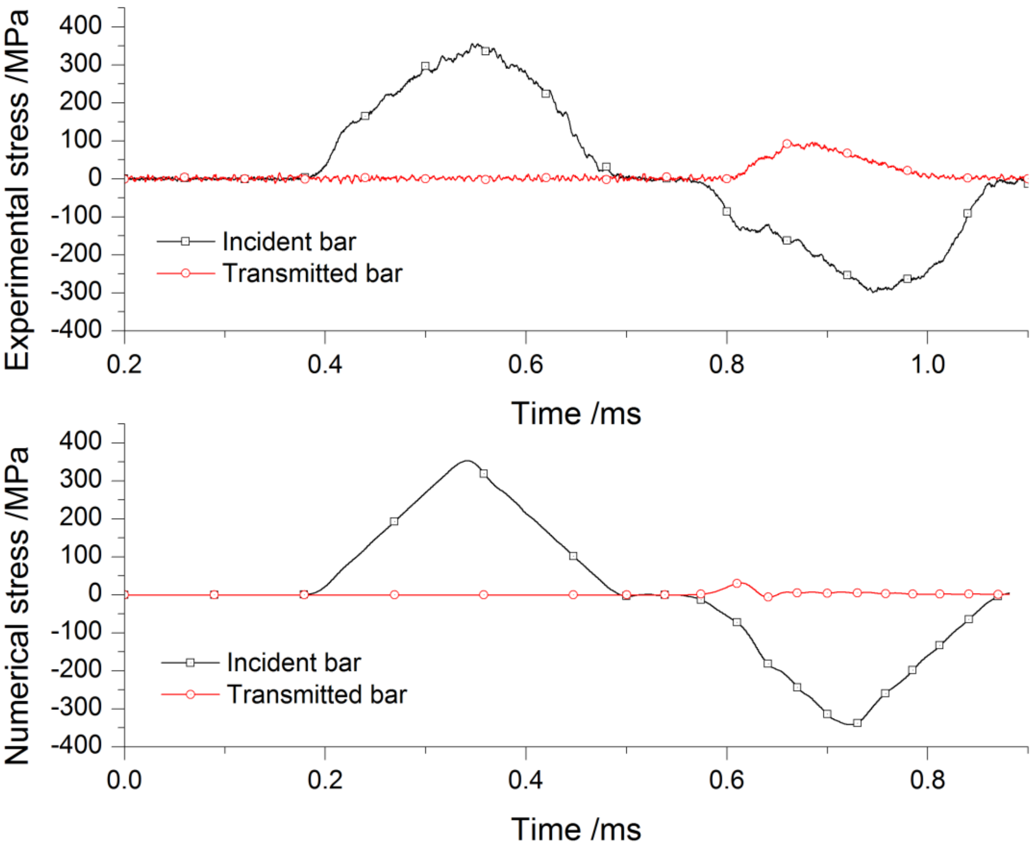

Figure 10 Experimental stress waves of the SHPB tests on the single-flawed marble, β = 30° (top) and simulated stress waves (bottom)

4.2 Cracking processes

In the cumulative damage model, the failure of a cell represents the development of a segment of a macro-crack. The damage model is found to be able to simulate the initiation and propagation of macro-cracks in the single-flawed specimen. In this model, the EPS1 and EPS2 are chosen to be 0.001 and 0.03, respectively, according to the experimental results. Other basic material properties are chosen to be identical in the numerical studies of quasi-static and dynamic tests. A lower friction coefficient at the interface between the specimen and the bar is used under dynamic loading [94].

4.2.1 Quasi-static loading

As shown in **Figure 11**B, the first cracks initiate at the flaw tips have the same positions as the tensile wing patches observed in the experimental study. With increasing loading, the propagation of the first cracks is limited, while two anti-wing cracks occur and propagate symmetrically around the flaw. Subsequently, shear cracks appear nearly at the same position as the first cracks do, but in different propagation direction. Finally, the development of the anti-wing cracks forming a diagonal crack band leads to specimen failure. In this period, the shear cracks propagate to a limited extent. The shear cracks and the anti-wing cracks constitute a diagonal failure band around the flaw, which agree with the experimental observation of the cracking processes (**Figure 9**).

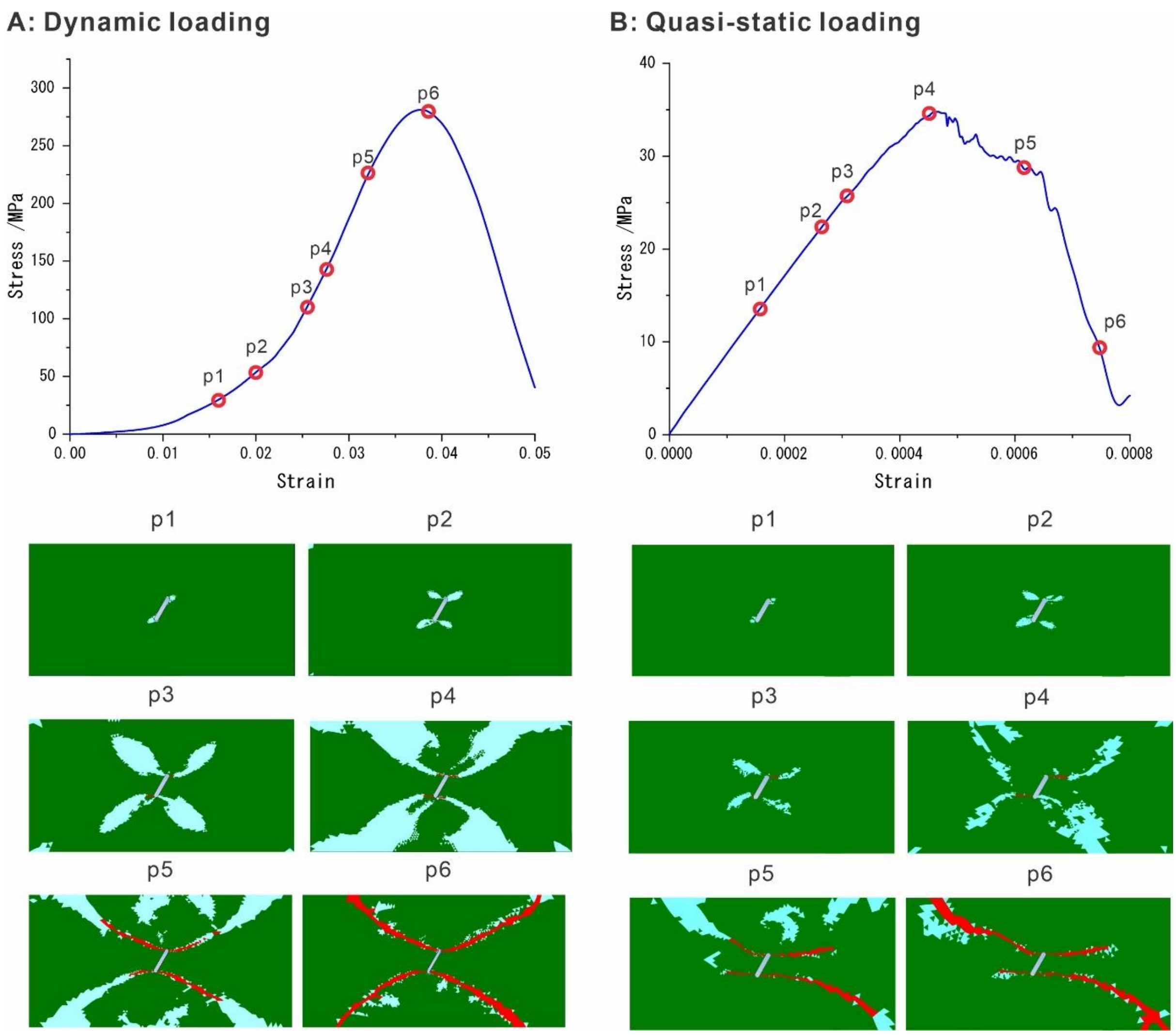

Figure 11 Stress-strain curve and the cracking processes under dynamic (A) and quasi-static (B) loadings in numerical studies (Red – cracks, Cyan – lower damage zone)

4.2.2 Dynamic loading

The simulation results of the dynamic test also well agree with the experimental cracking processes. **Figure 11**A shows the first cracks of the same specimen loaded dynamically. The geometry and position of the first cracks, which are also tensile wing cracks, under dynamic loading are similar to those under quasi-static loading. When the loading increases, the propagation of the first tensile wing cracks will be suppressed, and it changes its propagation direction and turns to be shear. The initiation and growth of the shear cracks and anti-wing cracks are favoured then. The shear and anti-wing crack patterns form an "X" shape. In contrast, the shear cracks are more developed than those under quasi-static loading. With the increase of the dynamic loading, both the shear cracks and anti-wing cracks develop preferentially. Consequently, an "X" shaped cracking mode dominates the specimen failure. Apart from the cracking behaviour, the simulated failure curves, as well as the failure strain, also show a similar result with the experiments. The simulated dynamic stress-strain curve is smoother and has a much higher failure strain, which implies the increase of ductileness under dynamic loading. This phenomenon is supported by the large-scale spreading of the plastic zone in the dynamic simulation too. The result indicates the validity of the present numerical model, including the material model and the failure criterion.

4.3 3D simulation

In order to verify whether the difference between 2D and 3D simulation result is acceptable, a 3D dynamic simulation is run and compared with the 2D result. The 3D simulation will consume nearly a hundred times of computation time even though the rectangular element and the relatively coarse element are used to improve the computation efficiency. The numerical model is shown in **Figure 12**. The cracking patterns on the specimen surface of the 3D simulation are generally similar to those of the 2D simulation. The 3D simulation result also indicates that the plane strain assumption is acceptable in the study of dynamic cracking processes using 2D FEM simulation.

The 3D simulation shows that the X shape failure mode appears not only on the front and reverse surfaces but also on the top and bottom surfaces. On the top and bottom surface, two diagonal cracking bands lead to the failure mode. The transparent view of the failure band show that the failure near the surface or the flaw boundary occurs first, and the side failure plane occurs consequently. It is caused by the unconfinement stress state on the free surface. The differences between the 2D and 3D simulations are minor but including (1) Relatively more branching cracks occur in the 3D simulation; (2) Similar X shape failure band occurs at the bottom surface in the 3D simulation; (3) The 3D failure zone around the pre-existing flaw is larger than the 2D condition

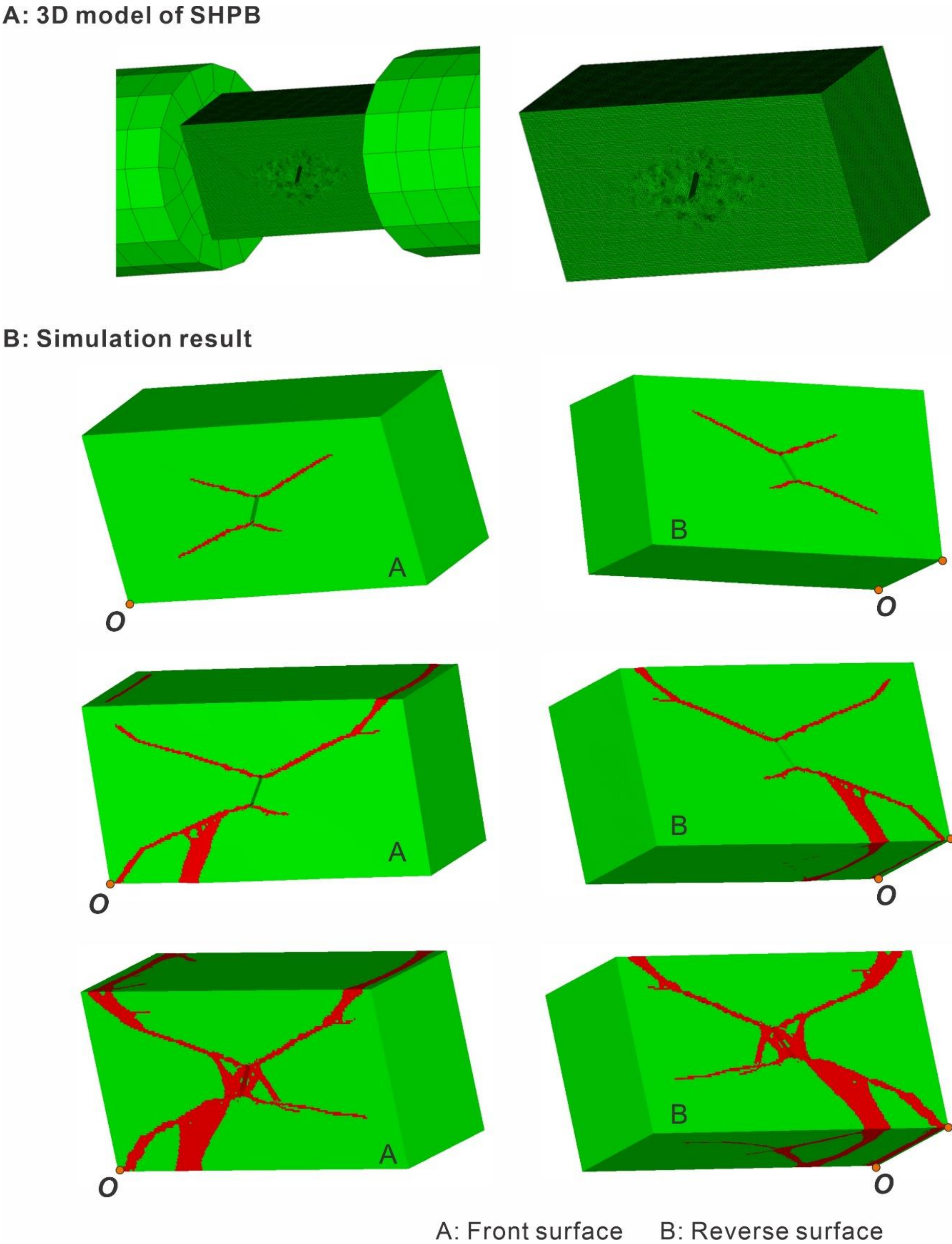

Figure 12 3D numerical model and the corresponding cracking processes of the single-flawed specimen

4.4 Summary

Similar to the experimental observation, the first cracks initiate at the flaw tips. It is due to the high stress concentration around the flaw tips and the low ratio of tensile strength to compressive strength for the Carrara marble. Even though the tensile strength has a higher rate-dependency than the compressive strength, the enhanced dynamic tensile strength is still significantly less than the dynamic compressive strength. Tensile cracks still appear first. After the initiation of the first cracks, the shear cracks initiate nearly simultaneously along with the secondary cracks. The further propagation of the first tensile cracks is suppressed under both loading conditions. The first tensile cracks evolve to shear cracks under dynamic loadings, while those under quasi-static loadings have minimal propagation. The former type of suppression leads to the "X" shaped failure mode under dynamic loadings, and the latter type of suppression leads to the diagonal failure mode under quasi-static loadings. In **Figure 13**, the numerical result of the specimens with other flaw inclination angles is compared with the experimental results under dynamic loading, which is reported in the author's previous paper. The comparison shows similar failure modes and proves the universal "X" shape failure mode under dynamic loading. The "X" shape failure mode shows independence on the flaw inclination angle for the single flawed specimen under dynamic loadings. This finding may provide some tips about the analysis of the historical forces on the pre-existing fractures, joints or faults. The historical loading rate of the forces can also be given by analyzing the crack patterns.

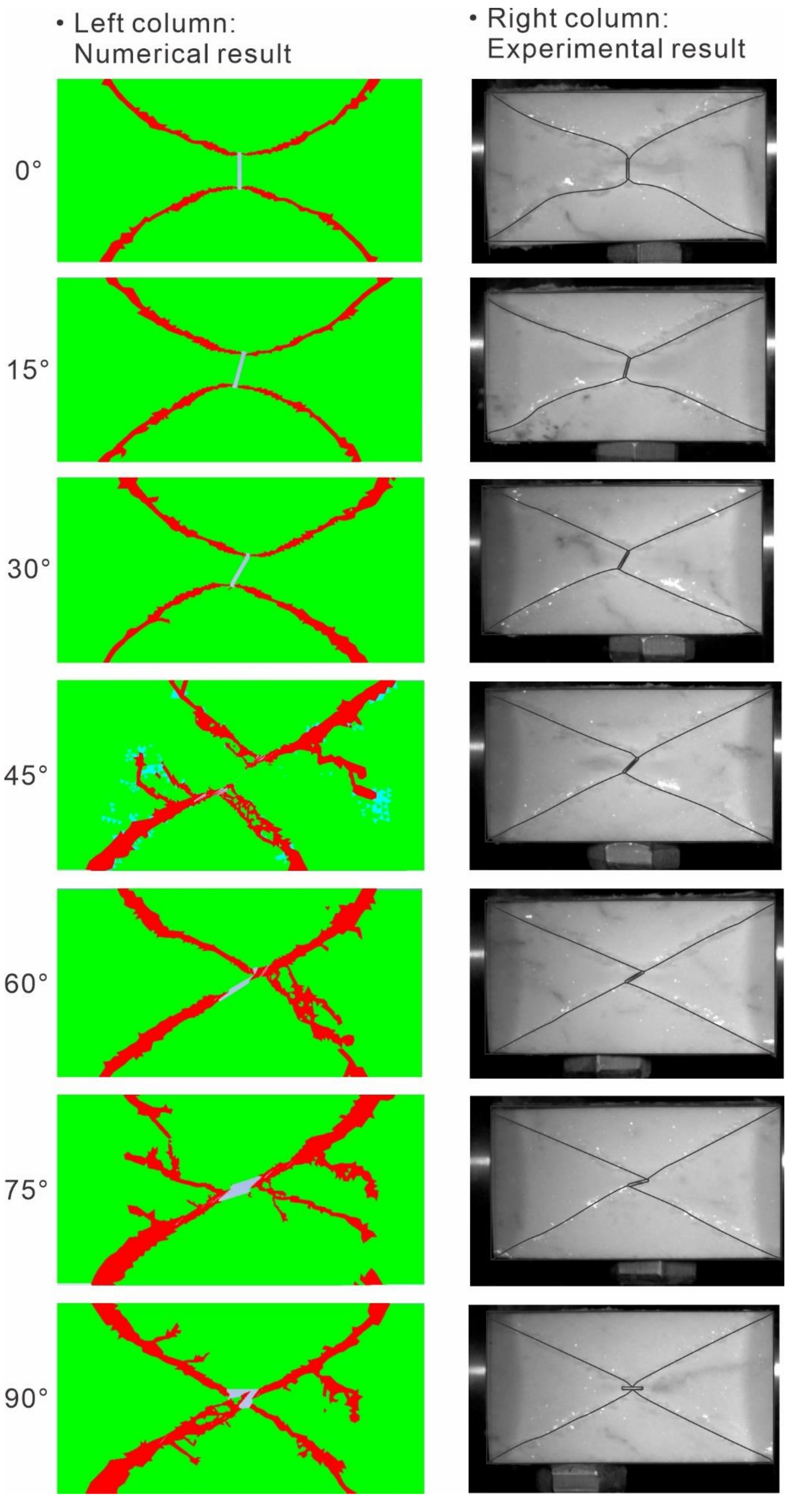

Figure 13 Failure modes of the single-flawed specimens with different flaw inclination angles in numerical and experimental results[59]

5. Discussion

5.1 Failure mode

From both the experimental and numerical results, the development of shear cracks under dynamic loading is more favoured than that under quasi-static loading. Furthermore, the remarkable growth of shear cracks with the growth of anti-wing cracks constitutes a symmetrical "X" shaped failure mode under dynamic loading [59]. From the displacement contour (**Figure 14**), a significantly higher displacement difference is found in the dynamic condition compared with the quasi-static condition. The result also indicates higher shear stress or strain under dynamic loadings, which dominates the failure of the specimen.

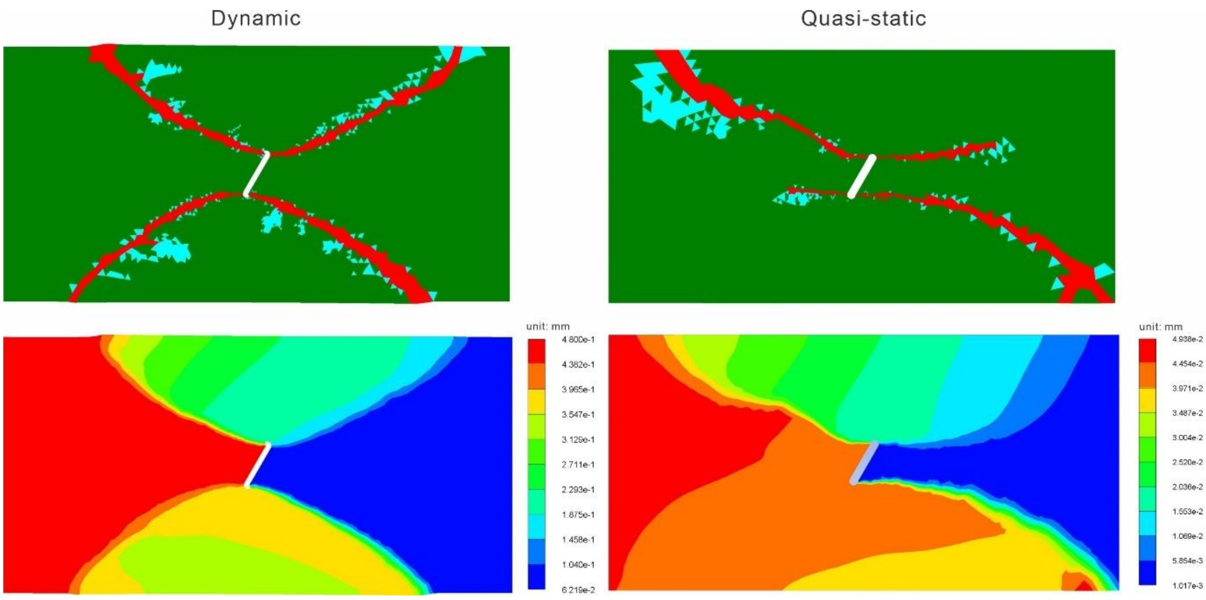

Figure 14 Failure mode and displacement contour under dynamic and quasi-static loadings in the numerical simulations

5.2 Suppression of the tensile wing patches

The tensile-wing patches are suppressed under dynamic loadings, which might be the result of a relatively higher tensile-compressive strength ratio under dynamic strain rates than that under quasi-static strain rates. In other words, the tensile strength increases faster than the compressive strength with the strain rate. The tests on the compressive dynamic increase factor (CDIF), which is the dynamic strength value normalized to the average quasi-static strength value, and tensile dynamic increase factor (TDIF) support this point. From the experimental results, around the dynamic strain rate of 150 s^{-1}, the TDIF is more than twice the CDIF. Therefore, for the same stress concentration factor, a higher TDIF will suppress the development of the tensile wing cracks. On the other hand, higher TDIF and lower CDIF will encourage the development of shear cracks.

5.3 Similar crack initiation

The stress concentration coefficient around the flaw depends on the geometry of the flaw and the specimen, not the loading rate and the material mechanical properties before the regional failure of the specimen. It is one of the reasons that account for the similar fracturing and deformation phenomena observed under different loading conditions, especially at the early stage of the cracking associated with the initiation of the white patches in Carrara marble. This point is also supported by the numerical results of the principal stress, as illustrated in **Figure 15**. However, the variation of TDIF and CDIF affects the resistance of propagation of different types of cracks.

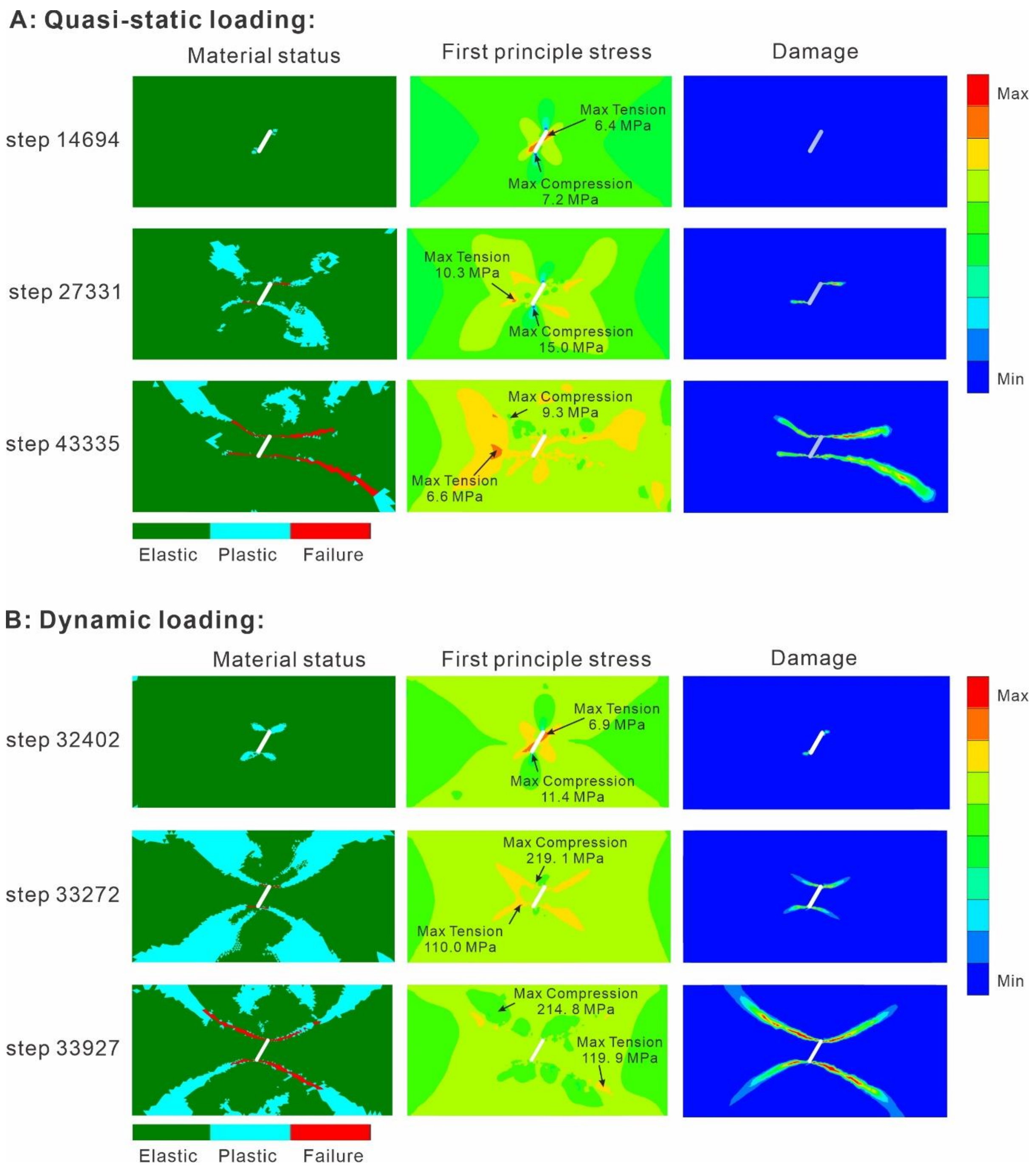

Figure 15 First principal stress and damage zone at different loading step in the quasi-static (A) and dynamic (B) loading simulation

5.4 Principal stress distribution and damage

Since both the tensile strength and the compressive strength increase with the strain rate, the maximum tensile and compressive stresses inside the specimen also increase significantly, especially in the stage of the crack propagation. The maximum dynamic tensile stress can be nearly ten times the quasi-static one, which is consistent with the dynamic strength increase factor (**Figure 15**). In the experimental result, the peak stress or strength of the single-flawed specimens also increases. The numerical result well explains why the failure stress on the specimen under dynamic loadings is much higher than that under quasi-static loadings.

The plastic zones do not always equal the damaged zone or the cracked zone. Early-stage loading can lead to the regional plastic zone, which is very similar to the white patches from the aspect of shape. However, since it is less than the EPS1, it is not a damaged zone. When the loading continues to increase, the stress keeps redistribution. More plastic zones appear and develop more. Only some of them remain the rising trend and reach the EPS1. These plastic zones become the damaged zone and finally evolve to the cracks. It means not all the white patches can develop into the macro-cracks.

5.5 Future work

The numerical study is performed based on the assumption that the different TDIF and CDIF at a specific dynamic strain rate affect the cracking behaviour of the marble specimens. However, other mechanical properties, which may also be strain rate-dependent, can also possibly affect the cracking behaviour. Further experimental and numerical investigations on other mechanical properties and their influences on fracturing are warranted. The preliminary 3D simulation also requires that the calculation efficiency should be enhanced by either better meshing methods or modified dynamic failure criterion. If this problem can be solved, the 3D simulation will be more applicable than the 2D one to obtain a more accurate result and more information in the special failure processes.

6. Conclusions

In the present paper, both experimental and numerical approaches are applied to study the different mechanical and fracturing behaviour in Carrara marble under quasi-static and dynamic loadings. Some conclusions and explanations for the rate-dependent differences can be made below.

1) The strain rate effect is significant on both compressive strength and tensile strength, while the dynamic tensile strength increases several times faster than the dynamic compressive strength with the strain rate.

2) The strain rate plays a decisive role in the development of macro-cracks and the failure modes of the single-flawed specimens.

3) Both the experimental and numerical studies reveal that the development of tensile-wing cracks is suppressed under the dynamic loadings, which coincides with the higher increase rate of the dynamic tensile strength. Shear cracks and anti-wing cracks are encouraged under dynamic loadings leading to the “X” shaped failure of the specimens despite the flaw inclination angle. Different increase rate between tensile and compressive strengths induces rate-dependent cracking behaviour.

4) The consistency between the experimental observation and the numerical simulation indicates that this material model and the dynamic D-P failure criterion have a potential application into more practical rock engineering projects. The 2D simulation is suitable to obtain reliable data and enough cracking process information compared with the 3D simulation.

5) The numerical plastic zones have nearly the same trajectories as the experimental observed white patches, which supports the origin of the white patch to be plastic zone.

Acknowledgement:

The data presented in this paper is obtained from the lab tests conducted by the authors in the Construction and Testing Laboratory at Nanyang Technological University. The authors appreciate the supervision and support of Prof. Ngai Yuen Wong, as well as the support of AcRF Tier 1 funding from the Ministry of Education, Singapore (RG 112/14) and the assistance of technician Weng Kong Cheng in the SHPB test in NTU. The authors are also grateful to the inspiring discussion with the group members headed by Prof. Jian Zhao in Monash University as well as the group members headed by Prof. Jianchun Li in Southeast University.

Reference:

1. Mishra S, Khetwal A, Chakraborty T. Dynamic Characterisation of Gneiss. *Rock Mechanics and Rock Engineering.* 2018;52(1): 61-81.

2. Levitas VI, Ravelo R. Virtual melting as a new mechanism of stress relaxation under high strain rate loading. *Proceedings of the National Academy of Sciences of the United States of America.* 2012;109(33): 13204.

3. Liao Z, Reches Ze. An experimentally-based friction law for high-velocity, long-displacement slip-pulse events during earthquakes. *Earth and Planetary Science Letters.* 2019;515: 209-220.

4. Xia K, Rosakis AJ, Kanamori H, Rice JR. Laboratory Earthquakes along Inhomogeneous Faults: Directionality and Supershear. *Science.* 2005;308(5722): 681-684.
5. Bao H, Ampuero J-P, Meng L, et al. Early and persistent supershear rupture of the 2018 magnitude 7.5 Palu earthquake. *Nature Geoscience.* 2019.
6. Gumbsch P, Gao H. Dislocations Faster than the Speed of Sound. *Science.* 1999;283(5404): 965-968.
7. Chi LY, Zhang ZX, Aalberg A, Yang J, Li CC. Fracture Processes in Granite Blocks Under Blast Loading. *Rock Mechanics and Rock Engineering.* 2019;52(3): 853-868.
8. Ngo T. Blast loading and blast effects on structures—an overview. *Electronic Journal of Structural Engineering.* 2007;Volume 7: 76-91.
9. Li J, Ma G, Zhou Y. Analytical Study of Underground Explosion-Induced Ground Motion. *Rock Mechanics and Rock Engineering.* 2012;45(6): 1037-1046.
10. Li JC, Li HB, Ma GW, Zhou YX. Assessment of underground tunnel stability to adjacent tunnel explosion. *Tunnelling and Underground Space Technology incorporating Trenchless Technology Research.* 2013;35: 227-234.
11. Liu P, Liu K, Zhang Q-B. Experimental characterisation of mechanical behaviour of concrete-like materials under multiaxial confinement and high strain rate. *Constr Build Mater.* 2020;258: 119638.
12. Li C, Li X, Liang L. Dynamic response of existing tunnel under cylindrical unloading wave. *Int J Rock Mech Min.* 2020;131: 104342.
13. Ma G, Hao H, Wang F. Simulations of explosion-induced damage to underground rock chambers. *J Rock Mech Geotech Eng.* 2011;3(1): 19-29.
14. Qian Q, Zhou X. Quantitative analysis of rockburst for surrounding rocks and zonal disintegration mechanism in deep tunnels. *J Rock Mech Geotech Eng.* 2011;3(1): 1-9.
15. Bischoff PH, Perry SH. Compressive behaviour of concrete at high strain rates. *Mater Struct.* 1991;24(6): 425-450.
16. Chen W, Song B, Chen WW. Kolsky Compression Bar Experiments on Brittle Materials. *Split Hopkinson (Kolsky) Bar.* Springer US; 2011:77-118.
17. Christensen R, Swanson S, Brown W. Split-hopkinson-bar tests on rock under confining pressure. *Experimental Mechanics.* 1972;12(11): 508-513.
18. Grote DL, Park SW, Zhou M. Dynamic behavior of concrete at high strain rates and pressures: I. experimental characterization. *International Journal of Impact Engineering.* 2001;25(9): 869-886.
19. Jiang FC, Vecchio KS. Dynamic effects in Hopkinson bar four-point bend fracture. *Metall Mater Trans A-Phys Metall Mater Sci.* 2007;38A(12): 2896-2906.
20. Li H, Li J, Zhao J. Laboratory compressive and tensile testing of rock dynamic properties. In: Zhao J, ed. *Advances in Rock Dynamics and Applications.* CRC Press; 2011:125-142.
21. Wang Q, Li W, Song X. A Method for Testing Dynamic Tensile Strength and Elastic Modulus of Rock Materials Using SHPB. *Pure and Applied Geophysics.* 2006;163(5): 1091-1100.
22. Dai F, Chen R, Xia K. A Semi-Circular Bend Technique for Determining Dynamic Fracture Toughness. *Experimental Mechanics.* 2010;50(6): 783-791.
23. Fengchun J, Ruitang L, Xiaoxin Z, Vecchio KS, Rohatgi A. Evaluation of dynamic fracture toughness KId by Hopkinson pressure bar loaded instrumented Charpy impact test. *Eng Fract Mech.* 2004;71(3): 279-287.
24. Wang QZ, Feng F, Ni M, Gou XP. Measurement of mode I and mode II rock dynamic fracture toughness with cracked straight through flattened Brazilian disc impacted by split Hopkinson pressure bar. *Eng Fract Mech.* 2011;78(12): 2455-2469.
25. Chunjiang Zou LNYW. Size and Geometry Effects on the Mechanical Properties of Carrara Marble Under Dynamic Loadings. *Rock Mechanics and Rock Engineering.* 2015: 1-12.
26. Bearman R, Briggs C, Kojovic T. The applications of rock mechanics parameters to the prediction of comminution behaviour. *Minerals engineering.* 1997;10(3): 255-264.
27. Banthia N, Mindess S, Bentur A, Pigeon M. Impact testing of concrete using a drop-weight impact machine. *Experimental Mechanics.* 1989;29(1): 63-69.
28. Whittles DN, Kingman S, Lowndes I, Jackson K. Laboratory and numerical investigation into the characteristics of rock fragmentation. *Minerals Engineering.* 2006;19(14): 1418-1429.

29. Shockey DA, Curran DR, Seaman L, Rosenberg JT, Petersen CF. Fragmentation of rock under dynamic loads. *International Journal of Rock Mechanics and Mining Sciences & Geomechanics Abstracts.* 11. Elsevier; 1974:303-317.
30. Grady DE, Kipp ME. The micromechanics of impact fracture of rock. *International Journal of Rock Mechanics and Mining Sciences & Geomechanics Abstracts.* 1979;16(5): 293-302.
31. Zhao J, Zhou YX, Hefny AM, et al. Rock dynamics research related to cavern development for ammunition storage. *Tunn Undergr Sp Tech.* 1999;14(4): 513-526.
32. Davies EDH, Hunter SC. The dynamic compression testing of solids by the method of the split Hopkinson pressure bar. *Journal of the Mechanics and Physics of Solids.* 1963;11(3): 155-179.
33. Frew D, Forrestal M, Chen W. A split Hopkinson pressure bar technique to determine compressive stress-strain data for rock materials. *Experimental Mechanics.* 2001;41(1): 40-46.
34. Kolsky H. An Investigation of the Mechanical Properties of Materials at very High Rates of Loading. *Proceedings of the Physical Society Section B.* 1949;62(11): 676.
35. Lok TS, Li XB, Liu D, Zhao PJ. Testing and response of large diameter brittle materials subjected to high strain rate. *J Mater Civ Eng.* 2002;14(3): 262-269.
36. Zhao J. An overview of some recent progress in rock dynamics research. In: Zhou Y, Zhao J, eds. *Advances in Rock Dynamics and Applications.* CRC Press; 2011:5-33.
37. Dai F, Xia K, Zheng H, Wang YX. Determination of dynamic rock Mode-I fracture parameters using cracked chevron notched semi-circular bend specimen. *Eng Fract Mech.* 2011;78(15): 2633-2644.
38. Zhou YX, Xia K, Li XB, et al. Suggested methods for determining the dynamic strength parameters and mode-I fracture toughness of rock materials. *Int J Rock Mech Min.* 2012;49(0): 105-112.
39. Zhang QB, Zhao J. Effect of loading rate on fracture toughness and failure micromechanisms in marble. *Eng Fract Mech.* 2013;102: 288-309.
40. Li XB, Lok TS, Zhao J. Dynamic Characteristics of Granite Subjected to Intermediate Loading Rate. *Rock Mechanics and Rock Engineering.* 2005;38(1): 21-39.
41. Toshiro K, Kenji M, Hideki I, Kenya M. Evaluation of static and dynamic fracture toughness in ceramics. *Eng Fract Mech.* 1988;31(5): 873-885.
42. Rubio L, Fernández-Sáez J, Navarro C. Determination of dynamic fracture-initiation toughness using three-point bending tests in a modified Hopkinson pressure bar. *Experimental Mechanics.* 2003;43(4): 379-386.
43. Chen C-S, Pan E, Amadei B. Determination of deformability and tensile strength of anisotropic rock using Brazilian tests. *Int J Rock Mech Min.* 1998;35(1): 43-61.
44. Cho SH, Ogata Y, Kaneko K. Strain-rate dependency of the dynamic tensile strength of rock. *Int J Rock Mech Min.* 2003;40(5): 763-777.
45. Zhao Y, Yang R, Chen C, Li Z, Liu Y, Ding L. Experimental Study on Impact Fracture of Side-Wing Offset Crack in Jointed Medium. 2021.
46. Meyers MA. *Dynamic behavior of materials / Marc A. Meyers*: New York ; Singapore : John Wiley & Sons, Inc., 1994.; 1994.
47. Meyers M, Gray G, Thadhani N. The dynamic behavior of materials: An introduction. *JOM Journal of the Minerals, Metals and Materials Society.* 2010;62(1): 14-15.
48. Grady DE, Kipp ME. Dynamic rock fragmentation. In: Atkinson B, ed. *Fracture Mechanics of Rocks.* NY: Academic Press; 1987.
49. Xu Y, Dai F, Xu NW, Zhao T. Numerical Investigation of Dynamic Rock Fracture Toughness Determination Using a Semi-Circular Bend Specimen in Split Hopkinson Pressure Bar Testing. *Rock Mechanics and Rock Engineering.* 2015: 1-15.
50. Yang S-Q, Huang Y-H, Tian W-L, Zhu J-B. An experimental investigation on strength, deformation and crack evolution behavior of sandstone containing two oval flaws under uniaxial compression. *Engineering Geology.* 2017;217(C): 35-48.
51. Zhang X-P, Zhang Q, Wu S. Acoustic emission characteristics of the rock-like material containing a single flaw under different compressive loading rates. *Computers and Geotechnics.* 2017;83: 83-97.

52. Zhang X-P, Wong L. Cracking Processes in Rock-Like Material Containing a Single Flaw Under Uniaxial Compression: A Numerical Study Based on Parallel Bonded-Particle Model Approach. *Rock Mechanics and Rock Engineering.* 2012;45(5): 711-737.
53. Zhou T, Zhu JB, Ju Y, Xie HP. Volumetric fracturing behavior of 3D printed artificial rocks containing single and double 3D internal flaws under static uniaxial compression. *Eng Fract Mech.* 2019;205: 190-204.
54. Zhou T, Zhu J. Mechanical and Volumetric Fracturing Behaviour of Three-Dimensional Printing Rock-like Samples Under Dynamic Loading. *Rock Mechanics and Rock Engineering.* 2020;53(6): 2855-2864.
55. Li X, Zhou T, Li D. Dynamic Strength and Fracturing Behavior of Single-Flawed Prismatic Marble Specimens Under Impact Loading with a Split-Hopkinson Pressure Bar. *Rock Mechanics and Rock Engineering.* 2017;50(1): 29-44.
56. Han Z, Li D, Zhou T, Zhu Q, Ranjith PG. Experimental study of stress wave propagation and energy characteristics across rock specimens containing cemented mortar joint with various thicknesses. *International journal of rock mechanics and mining sciences (Oxford, England : 1997).* 2020;131: 104352.
57. Li D, Han Z, Sun X, Zhou T, Li X. Dynamic Mechanical Properties and Fracturing Behavior of Marble Specimens Containing Single and Double Flaws in SHPB Tests. *Rock Mechanics and Rock Engineering.* 2019;52(6): 1623-1643.
58. Wong LNY, Zou C, Cheng Y. Fracturing and Failure Behavior of Carrara Marble in Quasistatic and Dynamic Brazilian Disc Tests. *Rock Mechanics and Rock Engineering.* 2014;47(4): 1117-1133.
59. Zou C, Wong LNY. Experimental studies on cracking processes and failure in marble under dynamic loading. *Engineering Geology.* 2014;173(0): 19-31.
60. Zou C, Wong LNY. Study of Mechanical Properties and Fracturing Processes of Carrara Marble in Dynamic Brazilian Tests by Two Optical Observation Methods. *Rock Mechanics and Its Applications in Civil, Mining, and Petroleum Engineering.* 2014:20-29.
61. Wong LNY, Einstein HH. Crack coalescence in molded gypsum and carrara marble: Part 1. macroscopic observations and interpretation. *Rock Mechanics and Rock Engineering.* 2009;42(Compendex): 475-511.
62. Coli M. Geomechanical characterisation of Carrara Marble. In: Balkema AA, ed. *ISRM Regional Symposium, EUROCK 2001.* Helsinky; 2001:53-57.
63. Rutter EH. Experimental study of the influence of stress, temperature, and strain on the dynamic recrystallization of Carrara marble. *Journal of Geophysical Research: Solid Earth.* 1995;100(B12): 24651-24663.
64. Fredrich JT, Evans B, Wong T-F. Micromechanics of the brittle to plastic transition in Carrara marble. *Journal of Geophysical Research: Solid Earth.* 1989;94(B4): 4129-4145.
65. Manchao H, Jia X, Coli M, Livi E, Sousa L. Experimental study of rockbursts in underground quarrying of Carrara marble. *Int J Rock Mech Min.* 2012;52: 1-8.
66. Huang J, Chen G, Zhao Y, Wang R. An experimental study of the strain field development prior to failure of a marble plate under compression. *Tectonophysics.* 1990;175(1-3): 269-284.
67. Li Y-P, Chen L-Z, Wang Y-H. Experimental research on pre-cracked marble under compression. *Int J Solids Struct.* 2005;42(9-10): 2505-2516.
68. Brooks Z, Ulm F, Einstein H, Abousleiman Y. A Nanomechanical Investigation of the Crack Tip Process Zone. *44th US Rock Mechanics Symposium and 5th US-Canada Rock Mechanics Symposium.* Salt Lake City, Utah, USA; 2010.
69. Brooks Z, Ulm FJ, Einstein HH. Role of microstructure size in fracture process zone development of marble. *46th U.S. Rock Mechanics/Geomechanics Symposium.* 3. Chicago, IL, USA; 2012:1748-1757.
70. Li H, Wong LNY. Influence of flaw inclination angle and loading condition on crack initiation and propagation. *Int J Solids Struct.* 2012;49(18): 2482-2499.
71. Hao Y, Hao H. Numerical Investigation of the Dynamic Compressive Behaviour of Rock Materials at High Strain Rate. *Rock Mechanics and Rock Engineering.* 2012: 1-16.
72. Ma GW, An XM. Numerical simulation of blasting-induced rock fractures. *Int J Rock Mech Min.* 2008;45(6): 966-975.

73. Hao Y, Hao H, Li Z-X. Numerical Analysis of Lateral Inertial Confinement Effects on Impact Test of Concrete Compressive Material Properties. *International Journal of Protective Structures.* 2010;1(1): 145-168.
74. Hao H, Ma G, Zhou Y. Numerical simulation of underground explosions. *Fragblast: International Journal for Blasting and Fragmentation.* 1998;2(4): 383-395.
75. Huang D, Gu D, Yang C, Huang R, Fu G. Investigation on Mechanical Behaviors of Sandstone with Two Preexisting Flaws under Triaxial Compression. *Rock Mechanics and Rock Engineering.* 2015: 1-25.
76. Jaeger JC, Cook NGW, Zimmerman RW. *Fundamentals of rock mechanics [electronic resource] / J.C. Jaeger, N.G.W. Cook, and R.W. Zimmerman*: Malden, MA : Blackwell Pub., 2007. 4th ed.; 2007.
77. Colmenares LB, Zoback MD. A statistical evaluation of intact rock failure criteria constrained by polyaxial test data for five different rocks. *Int J Rock Mech Min.* 2002;39(6): 695-729.
78. Menetrey P, Willam K. Triaxial failure criterion for concrete and its generalization. *Aci Struct J.* 1995;92(3): 311-318.
79. Seltzer R, Cisilino AP, Frontini PM, Mai Y-W. Determination of the Drucker–Prager parameters of polymers exhibiting pressure-sensitive plastic behaviour by depth-sensing indentation. *International Journal of Mechanical Sciences.* 2011;53(6): 471-478.
80. Darlington WJ, Ranjith PG, Choi S. The Effect of Specimen Size on Strength and Other Properties in Laboratory Testing of Rock and Rock-Like Cementitious Brittle Materials. *Rock Mechanics and Rock Engineering.* 2011;44(5): 513-529.
81. Pankow M, Attard C, Waas AM. Specimen size and shape effect in split Hopkinson pressure bar testing. *J Strain Anal Eng Des.* 2009;44(8): 689-698.
82. Wong LNY, Zou C. Cracking processes in rocks under dynamic loading. *7th Asian Rock Mechanics Symposium, an ISRM regional symposium.* Seoul, Korea; 2012:485-494.
83. Bieniawski ZT, Bernede MJ. Suggested methods for determining the uniaxial compressive strength and deformability of rock materials: Part 1. Suggested method for determining deformability of rock materials in uniaxial compression. *International Journal of Rock Mechanics and Mining Sciences & Geomechanics Abstracts.* 1979;16(2): 138-140.
84. Bieniawski Z, Hawkes I. Suggested methods for determining tensile strength of rock materials. *Int J Rock Mech Mng Sci & Geomech Abstr.* 1978;15: 99-103.
85. Ravichandran G, Subhash G. CRITICAL-APPRAISAL OF LIMITING STRAIN RATES FOR COMPRESSION TESTING OF CERAMICS IN A SPLIT HOPKINSON PRESSURE BAR. *J Am Ceram Soc.* 1994;77(1): 263-267.
86. Chen W, Song B, Chen WW. Testing Conditions in Kolsky Bar Experiments. *Split Hopkinson (Kolsky) Bar.* Springer US; 2011:37-75.
87. Vecchio KS, Jiang FC. Improved pulse shaping to achieve constant strain rate and stress equilibrium in split-hopkinson pressure bar testing. *Metall Mater Trans A-Phys Metall Mater Sci.* 2007;38A(11): 2655-2665.
88. Wang L, Zhao J, Hua A, Zhao X. Research on SHPB testing technique for brittle material. *Yanshilixue Yu Gongcheng Xuebao/Chinese Journal of Rock Mechanics and Engineering.* 2003;22(Compendex): 1798-1802.
89. Frew DJ, Forrestal MJ, Chen W. Pulse shaping techniques for testing brittle materials with a split Hopkinson pressure bar. *Experimental Mechanics.* 2002;42(1): 93-106.
90. Li XB, Lok TS, Zhao J, Zhao PJ. Oscillation elimination in the Hopkinson bar apparatus and resultant complete dynamic stress–strain curves for rocks. *Int J Rock Mech Min.* 2000;37(7): 1055-1060.
91. Persson A. CM 1- A SIMPLE MODEL FOR THE DYNAMIC DEFORMATION AND FAILURE PROPERTIES OF BRITTLE MATERIALS. *4 th Int. Symp. Ceramic Materials and Components for Engines Goteborg.* 10. 1991.
92. Haimson B. True Triaxial Stresses and the Brittle Fracture of Rock. In: Dresen G, Zang A, Stephansson O, eds. *Rock Damage and Fluid Transport, Part I.* Birkhäuser Basel; 2006:1101-1130.
93. Wong LNY, Einstein HH. Systematic evaluation of cracking behavior in specimens containing single flaws under uniaxial compression. *Int J Rock Mech Min.* 2009;46(Compendex): 239-249.

94. Olsson H, Åström KJ, Canudas de Wit C, Gäfvert M, Lischinsky P. Friction Models and Friction Compensation. *European Journal of Control*. 1998;4(3): 176-195.